Latorre, M.; Romero, X.; Montáns, FJ. (2016). The relevance of transverse deformation effects in modeling soft biological tissues. International Journal of Solids and Structures. 99:57-70. https://doi.org/10.1016/j.ijsolstr.2016.08.006

The relevance of transverse deformation effects in modeling soft biological tissues

Marcos Latorre, Xabier Romero, Francisco J. Montáns*

Escuela Técnica Superior de Ingeniería Aeronáutica y del Espacio
Universidad Politécnica de Madrid
Plaza Cardenal Cisneros, 3, 28040-Madrid, Spain

Abstract

Hyperelastic constitutive models for anisotropic biological materials are frequently based on orthotropic incompressible stored energy functions. The material parameters of these models are then obtained through an optimization procedure as to fit some stress-strain experimental data. For example, in arterial wall mechanics the material data usually employed for the Holzapfel-Gasser-Ogden and the Gasser-Ogden-Holzapfel models are two uniaxial tension curves from circumferential and axial specimens. The transverse strains from these specimens are frequently not taken into consideration. In this paper we analyze the evolution of those strains, showing that an unrealistic behaviour may be predicted. We then show how transverse strains may be prescribed using our What-You-Prescribe-Is-What-You-Get (WYPIWYG) model in a very intuitive way, still capturing the longitudinal stress-strain behavior in an exact manner without employing any constitutive parameter. This is possible because, in contrast to what it is usually done, we exactly solve the equilibrium and compatibility equations without imposing the shape of the stored energy function. Furthermore, we show that the small strains formulation is naturally recovered and that the physical insight from the infinitesimal theory is preserved. In fact, for incompressible materials, the present approach can be considered as a natural extension of the infinitesimal continuum elastic framework to large strains. This new physical insight clearly shows that if some subclasses of orthotropic incompressible material models are determined with just two uniaxial curves, then the transverse behavior should be contrasted with additional experimental observations.

*Corresponding author. Tel.:+34 913 366 367.
Email addresses: m.latorre.ferrus@upm.es (Marcos Latorre), xabier.romero@upm.es (Xabier Romero), fco.montans@upm.es (Francisco J. Montáns)

Keywords: Composites; Biological tissues; orthotropy; hyperelasticity; arterial wall mechanics; transverse strains.

1. Introduction

In contrast to the usual approach employed in fiber-reinforced industrial composites, where a linear small strain analysis is performed [1], in soft biological tissues large strain measures and associated constitutive equations are employed because the behavior is highly nonlinear. Then, the first modelling approach to soft biological (collagen-reinforced) tissues is to employ hyperelastic constitutive models [2, 3]. However, hyperelastic (true elastic, path independent) behavior puts some restrictions in the constitutive equations which, for the linear model, are simply fulfilled by the symmetries of the constitutive tensor. In order to also automatically fulfill these restrictions in the nonlinear regime, authors typically propose a stored energy function shape; the shape being modulated by some material parameters as to fit (with variable success) some experimental data [4]. For isotropic materials, many constitutive models have been proposed (see [5, 6, 7, 8, 9, 10] among others), and usually, the linear infinitesimal theory may be recovered and the infinitesimal moduli easily related to the material parameters as, for example, in the Ogden model [10].

In the case of transverse isotropic and orthotropic materials, several proposals are also available and frequently used in soft biological tissues, some of them phenomenological in approach as the popular Fung model [11, 12] (see also [13]), and some using microstructure information, see for example [14, 15, 16, 17, 18, 19, 20, 21, 22, 23, 24, 25, 26, 27, 28, 29]. In these models a frequent approach to preserve frame invariance in general is to establish the stored energy as a function of Spencer's pseudo-invariants of the right Cauchy-Green metric tensor [30]. Then, to arrive at workable formulations, some of these invariants are frequently neglected [31], see discussion in [32], and because the meaning of some of these invariants is not intuitive, the consequences may be unexpected, as we show below. Moreover, it is usual the case where the material parameters are also of difficult interpretation, and the problem encountered in finding the best solution for isotropic materials [33, 52], is magnified in anisotropic ones [19, 60]. Then, material symmetries congruency may not be obtained either theoretically or computationally [34], so the predictions for an isotropic material characterized with these models may result in that of an anisotropic material. Some requirements regarding this issue for stored energies based on Cauchy–Green invariants may be found in the paper of Murphy [35].

Furthermore, a relevant point recently analyzed also by Murphy is that the proposed anisotropic models do not recover the full infinitesimal orthotropic theory [35]. In fact, for someone not acquainted with biomechanics constitutive models but with fiber-reinforced composites background, it may be surprising that an incompressible orthotropic material may be fully characterized with just two tension curves [28, 36], when the linear fiber-reinforced elastic counterpart needs six independent moduli (i.e. six slopes of six independent curves), see [32]. Then, in these models the effects of transverse strains are either neglected, ignored or assumed to be correctly given *by the model* (but usually never verified) and the result may be rather unexpected [23]. It is obvious, even from the infinitesimal theory, that transverse strains are very important in 3D or 2D constrained analyses, so if transverse strains are not correctly captured, in general it is to be expected that the longitudinal behavior will neither be correctly predicted in a configuration different from the uniaxial test. General requirements on stored energies based on Cauchy–Green invariants in order to recover the full infinitesimal theory are given in [35]. A consequence of not fulfilling these requirements may be the inability of the model to properly represent a general incompressible orthotropic material not only under infinitesimal strains but also under large deformations. Indeed, for the case of arteries, it has been recently shown that predictions of Poisson's ratio with some widely used models initially developed for these type of biological materials are inconsistent with experimental data [37]. In summary, apart from the challenging interpretation of the invariants and material parameters being used (which are usually obtained from optimization procedures), and assuming that the compression behavior of fibers is properly accounted for [38], the following difficulties are frequently found in these models: non-uniqueness of material parameters [33, 19, 60], inconsistency with the equivalent full linear theory [35], lack of numerical material symmetries congruency [34] and unrealistic transverse strains [37].

In order to overcome all these difficulties, we have recently presented two hyperelasticity models in the realm of the WYPIWYG (What-You-Prescribe-Is-What-You-Get) approach, an approach which we also applied to viscoelasticity [39, 40] and damage [41]. One of the hyperelastic models is for transverse isotropic materials [42], see also Ref. [43], and the other one for orthotropic materials [44]. The formulations are based on the isotropic incompressible model of Sussman and Bathe [45], which is already available in the commercial finite element code ADINA [46]. These models are purely phenomenological, i.e. no information about the structure of the material is employed, except for the material symmetries. Furthermore, the models use meaningful, easy-to-interpret invariants of the logarithmic strains [47], which are a natural extension of infinitesimal strains. In fact, we show here that

the formulation itself may be understood as a natural extension of the infinitesimal model to large strains because we use the same uncoupled form for the stored energy as that of the infinitesimal framework and because logarithmic strains have unique properties parallel to those of infinitesimal strains. For example, they are additive if the principal strain directions remain fixed, the push-forward and pull-back operations are performed with the rotation part of the deformation gradient (i.e. they preserve the metric with respect both the reference and the current configurations) and the deviatoric and volumetric operators are the same as those of the infinitesimal theory. Discussions on the properties of logarithmic strains and their relation with infinitesimal strains can be found in [47, 48, 49, 50, 51], among others. As a result, six curves (including the compression part when applicable [52]) are needed to fully characterize our orthotropic model. These curves are exactly captured, close to the machine precision, with the modified algorithm given below, and uniquely determine the six reference elastic moduli and their evolution. With the previous algorithm, presented in [44], the solution was not obtained in an strictly exact manner (computationally speaking), although the solution could be considered exact for practical purposes if the tendency of the transverse deformations, e.g. linear, quadratic, etc., is known from experimental measurements [37]. However, the new algorithm yields exact solutions which will be useful for the current analysis and without employing user-prescribed starting values. Furthermore, as we also show below, insight into the behavior of the model under finite strains is naturally and accurately obtained by an analysis of the infinitesimal theory. This insight is also crucial in order to be able to prescribe the possibly unknown (in a quantitative manner) transverse finite strains such that the behavior is according to what one would physically expect (in a qualitative manner). In our opinion, this is a much better option for unknown curves than to simply ignore them.

The rest of the paper is structured as follows. We first analyze the transverse strains under uniaxial tests obtained, just as examples, by two well-known and widely used models: the Holzapfel-Gasser-Ogden model [19] and the Gasser-Ogden-Holzapfel model [23]. However we emphasize that similar situations may be present in other simplified models when transverse strains are not explicitly considered, as the experiments of Skacel and Bursa [37] show. Then we explain the new computational procedure for the Latorre-Montáns model [44] which exactly captures the prescribed experimental non-linear curves, a procedure which uses the insight given by the infinitesimal model. Furthermore, we then show that this insight allows for the prediction beforehand of additional transverse strain distributions and also their influence in the third direction, showing a behavior under finite strains similar to that of the small strains theory. We finally demonstrate that the same axial and

circumferential stress predictions over the arterial wall may be exactly obtained with different stored energies if different transverse strains are prescribed; i.e. a real, general orthotropic incompressible material is not correctly characterized in preferred material directions using only two curves, even if they are exactly captured, as it is immediately deduced from the linear theory. Only particular cases of orthotropy may be represented with those stored energies. Then, the adequacy of those hypothesis to represent the actual material behavior of the specific materials at hand should be tested [37, 32].

2. Holzapfel–Gasser–Ogden aligned fiber model

In this section we study the mechanical behavior of arterial wall specimens under uniaxial testing using the well-known model of Holzapfel, Gasser and Ogden [19], usually referred to as the HGO model. This model is also similar to that given in Eqs. (13) and (20c) of [15]; see also therein references for motivation. The main purpose in this section is to analyse the transverse deformation patterns *given* by the model in uniaxial testing. It will be assumed (throughout this work) that the arterial wall deformation is purely isochoric.

The most general form of the HGO hyperelastic model for purely incompressible materials depends on seven invariants obtained from the right Cauchy–Green isochoric deformation tensor $\bar{\boldsymbol{C}}$: two of them being isotropic invariants and the remaining five being anisotropic pseudo-invariants, see Eq. (62) in Ref. [19]. The second-order tensor $\bar{\boldsymbol{C}}$ is defined using the isochoric deformation gradient tensor $\bar{\boldsymbol{X}}$ resulting from the Flory decomposition of the total deformation gradient $\boldsymbol{X} =: J^{1/3}\bar{\boldsymbol{X}} =: \det(\boldsymbol{X})^{1/3}\bar{\boldsymbol{X}}$ as $\bar{\boldsymbol{C}} = \bar{\boldsymbol{X}}^T\bar{\boldsymbol{X}}$. However, if the number of available experimental curves are insufficient to properly define an orthotropic model including all the independent invariants, it is frequent the case where the number of invariants and material parameters that describe the corresponding strain energy function is reduced [32]. For example, the model of Eq. (62) in Ref. [19] is further simplified and formulated in terms of one isotropic invariant $\bar{I}_1$ and two anisotropic invariants $\bar{I}_4$ and $\bar{I}_6$, see Eq. (63) in Ref. [19]. This simpler decomposition was originally considered sufficiently general to describe the arterial mechanical response [19], hence being the most frequently (simplified) version of the HGO model encountered in the literature and also recently considered "the most influential model to be developed in the last 20 years for modelling biological tissues" [53].

At this point, we note that there is nothing wrong in neglecting the contribution of some invariants. Approximations are frequently sought and desired in engineering problems and performed in soft tissues because of practical reasons, see analysis

in [32]. For example, in the transversely isotropic model of the myocardium due to Humphrey et al. [16, 17], only the invariants $\bar{I}_1$ and $\bar{I}_4$ were used, whereas the remaining $\bar{I}_2$ and $\bar{I}_5$ were dropped. This simplification allowed them to use two invariants, making both the experimental design and the computational model tractable. No inability to reproduce the (available) data was observed. However, approximations of this type may be more questionable in the orthotropic case because more invariants are involved. In any case, and this is the point of this analysis, simplifications regarding the number of selected invariants should never result in unrealistic responses, as the ones we show below, or go against experimental evidences, as the ones recently measured in Ref. [37]. That unrealistic behavior should be prevented when performing such approximations.

The HGO model was also employed to analyze the mechanical behavior of arterial specimens under uniaxial testing with consideration of fiber dispersion. Hereafter we use the notation of Ref. [23]. The strain energy function $\mathcal{W}$ associated to the simplified HGO model includes two main contributions. The first contribution, $\mathcal{W}_g$, accounts for the purely isotropic behavior of the matrix constituent (mainly elastin), and the second one, $\mathcal{W}_f$, accounts for the anisotropic contribution associated to the (collagen) fibres within the artery. Since arteries present two preferred referential directions $\boldsymbol{a}_{01}$ and $\boldsymbol{a}_{02}$ about which the fibers are preferentially aligned, the anisotropic contribution is additively split as $\mathcal{W}_f = \sum_{i=1}^{2} \mathcal{W}_{fi}$, with $\mathcal{W}_{fi}$ describing the mechanical behavior of the ith aligned fiber family. The groundmatrix strain energy function $\mathcal{W}_g$ is formulated in Refs. [19], [23] by means of the incompressible neo-Hookean model

$$\mathcal{W}_g(\bar{I}_1) = \frac{c}{2}(\bar{I}_1 - 3) \tag{1}$$

where $\bar{I}_1 = \text{tr}\ \bar{\boldsymbol{C}} = \boldsymbol{I} : \bar{\boldsymbol{C}}$ is the first principal invariant of $\bar{\boldsymbol{C}}$ and c is the (shear modulus alike) neo-Hookean parameter. Each transversely isotropic stored energy function $\mathcal{W}_{fi}$ is represented by the same Fung-type exponential function —as in Ref. [23] we consider $\bar{I}_{41} \equiv \bar{I}_4$ and $\bar{I}_{42} \equiv \bar{I}_6$

$$\mathcal{W}_{fi}(\bar{I}_{4i}) = \mathcal{W}_f(\bar{I}_{4i}) = \frac{k_1}{2k_2}\left[\exp\left(k_2(\bar{I}_{4i} - 1)^2\right) - 1\right] \tag{2}$$

where k_1 and k_2 are material parameters and the invariant $\bar{I}_{4i} = \boldsymbol{a}_{0i} \otimes \boldsymbol{a}_{0i} : \bar{\boldsymbol{C}}$ represents the squared stretch of the fiber initially oriented about the referential direction $\boldsymbol{a}_{0i}$.

2.1. Uniaxial testing

We obtain now numerical results from uniaxial tensile tests performed over arterial wall specimens using the HGO model. We consider the material parameters $c = 7.64\,\text{kPa}$, $k_1 = 996.6\,\text{kPa}$ and $k_2 = 524.6$, which are taken from Ref. [23]. When used with the aligned model of Eq. (2), these material parameters do not describe the mechanics of advential tissue [23]. However, as in that Reference, we use these specific values for comparison purposes. The angle $\gamma = 90^o - 49.98^o = 40.02^o$ defines the orientation of both fibers in the arterial wall reference frame $X_{123} = \{1, 2, 3\}$ of Figure 1 through $\boldsymbol{a}_{01} = [\cos\gamma, -\sin\gamma, 0]$ and $\boldsymbol{a}_{02} = [\cos\gamma, \sin\gamma, 0]$, where we have changed the definition of the angle γ with respect to Ref. [23] for the matter of convenience in the model definition of Section 4. The axial and circumferential specimens to be tested are also shown in that figure. The uniaxial tensile tests over the axial and circumferential specimens are separately performed along Axis 1 (with the stretch $\lambda_1 \geq 1$) and 2 (for which $\lambda_2 \geq 1$), respectively. The modified [19, 31] second Piola–Kirchhoff stresses $\bar{\boldsymbol{S}} = 2\partial\mathcal{W}/\partial\bar{\boldsymbol{C}}$ that directly derive from the total strain energy function $\mathcal{W} = \mathcal{W}_g + \sum_{i=1}^{2}\mathcal{W}_{fi}$ are

$$\bar{\boldsymbol{S}} = 2\frac{\partial\mathcal{W}_g}{\partial\bar{I}_1}\frac{\partial\bar{I}_1}{\partial\bar{\boldsymbol{C}}} + \sum_{i=1}^{2} 2\frac{\partial\mathcal{W}_{fi}}{\partial\bar{I}_{4i}}\frac{\partial\bar{I}_{4i}}{\partial\bar{\boldsymbol{C}}} = c\boldsymbol{I} + 4k_1(\bar{I}_4 - 1)\exp\left[k_2(\bar{I}_4 - 1)^2\right]\boldsymbol{A}_0 \qquad (3)$$

where $\boldsymbol{A}_0 := \frac{1}{2}\sum_{i=1}^{2}\boldsymbol{a}_{0i}\otimes\boldsymbol{a}_{0i}$ and the invariants $\bar{I}_1$ and $\bar{I}_4 := \bar{I}_{41} = \bar{I}_{42}$ are given by

$$\bar{I}_1 = \lambda_1^2 + \lambda_2^2 + 1/\left(\lambda_1^2\lambda_2^2\right) \qquad (4)$$

$$\bar{I}_4 = \lambda_1^2\cos^2\gamma + \lambda_2^2\sin^2\gamma \qquad (5)$$

where note that the incompressibility constraint $\lambda_1\lambda_2\lambda_3 = 1$ has been used in the expression of $\bar{I}_1$ —even though it is not present in the second identity in Eq. (3). The only non-vanishing components of the second-order tensor $\boldsymbol{A}_0$ in Identity $(3)_2$, expressed in the reference frame $X_{123} = \{1, 2, 3\}$ of Figure 1, are $(A_0)_{11} = \cos^2\gamma$ and $(A_0)_{22} = \sin^2\gamma$. The true, total Cauchy stresses are readily obtained from the fictitious second Piola–Kirchhoff stresses $\bar{\boldsymbol{S}}$ of Eq. (3) and the isochoric deformation gradient tensor $\bar{\boldsymbol{X}} = \text{diag}\,[\lambda_1, \lambda_2, 1/(\lambda_1\lambda_2)]$ through $\boldsymbol{\sigma} = \bar{\boldsymbol{X}}\bar{\boldsymbol{S}}\bar{\boldsymbol{X}}^T + p\boldsymbol{I}$, where p is an additional hydrostatic pressure to be obtained from the equilibrium equations and boundary conditions of the respective uniaxial test under consideration, cf. Ref. [38].

For the uniaxial tensile test performed over the axial specimen (Axis 1 in Figure 1, $\lambda_1 \geq 1$), the boundary conditions are $\sigma_2 = \sigma_3 = 0$. After eliminating the pressure

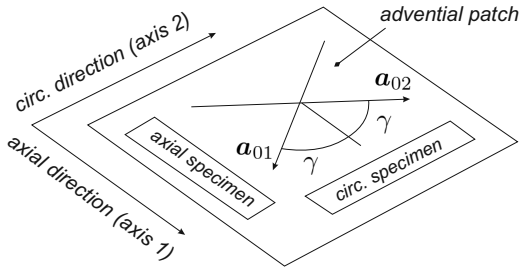

Figure 1: Definition of axial and circumferential specimens for the tensile tests and global axes numeration. Axis 3 (perpendicular to the advential patch) represents the artery radial direction. $\gamma = 90^o - 49.98^o = 40.02^o$.

from the system of equations $\boldsymbol{\sigma} = \bar{\boldsymbol{X}}\bar{\boldsymbol{S}}\bar{\boldsymbol{X}}^T + p\boldsymbol{I}$, we arrive at

$$\sigma_1 = c\left(\lambda_1^2 - \frac{1}{\lambda_1^2\lambda_2^2}\right) + 4k_1(\bar{I}_4 - 1)\exp\left[k_2(\bar{I}_4 - 1)^2\right]\lambda_1^2\cos^2\gamma \tag{6}$$

$$0 = c\left(\lambda_2^2 - \frac{1}{\lambda_1^2\lambda_2^2}\right) + 4k_1(\bar{I}_4 - 1)\exp\left[k_2(\bar{I}_4 - 1)^2\right]\lambda_2^2\sin^2\gamma \tag{7}$$

where Eq. (5) is to be used. Equations (6) and (7) can be solved numerically for each stretch $\lambda_1 > 1$ to give the uniaxial (axial) stress $\sigma_1(\lambda_1)$ and the transverse (circumferential) stretch $\lambda_2(\lambda_1)$. More specifically, we can obtain the transverse stretch $\lambda_2(\lambda_1)$ directly from Eq. (7) and then substitute in Eq. (6) to obtain the corresponding stress $\sigma_1(\lambda_1)$. The computed solution variables σ_1 and λ_2, together with the radial stretch $\lambda_3 = 1/(\lambda_1\lambda_2)$, are shown in Figure 2 for the range $\lambda_1 \in [0, 1.228]$ (the value $\lambda_1 = 1.228$ is taken so that $(\sigma_1)_{max} \approx 10\,\text{MPa}$ in Section 3). As a result of these calculations, it is obtained that the invariant $\bar{I}_4$ is always greater than one for each value of the axial stretch $\lambda_1 > 1$, see the case labelled as $\kappa = 0$ in Figure 4 of Ref. [38], hence fibers are always in extension and no tension-compression switch is needed in this case.

The results regarding the uniaxial test over the circumferential strip (Axis 2 in Figure 1, $\lambda_2 \geq 1$), which boundary conditions are $\sigma_1 = \sigma_3 = 0$, are shown in Figure 3 for $\lambda_2 \in [0, 1.32]$. Again, the invariant $\bar{I}_4$ is always greater than one in this test, see the case labelled as $\kappa = 0$ in Figure 3 of Ref. [38].

In Figures 2 and 3 we can observe that the radial stretch λ_3 is greater than one after some deformation level, i.e. the thickness of both specimens increases with respect to the initial thickness when both strips are subjected to tensile tests. This could be considered an unexpected, unrealistic result. Indeed, these nonphysical

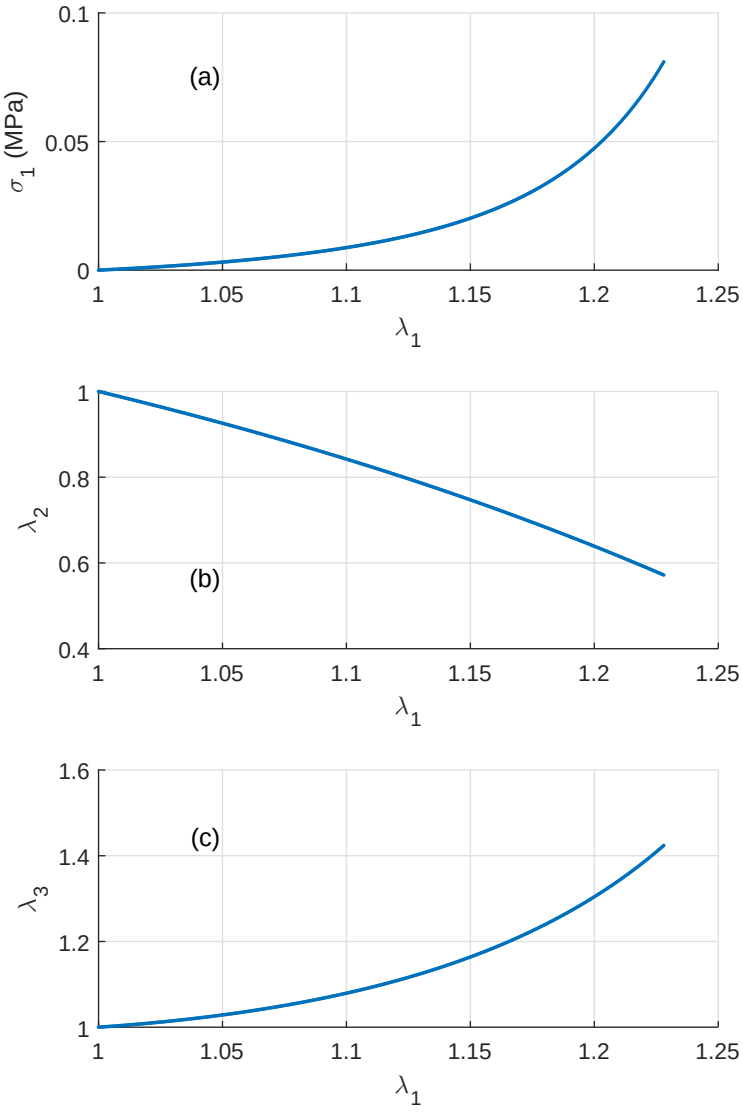

Figure 2: Uniaxial test over the axial specimen (direction 1 in Figure 1) using the model of Section 2. (a) Uniaxial stress in axial direction σ_1 (b) Transverse stretch in circumferential direction λ_2 (c) Transverse stretch in radial direction λ_3.

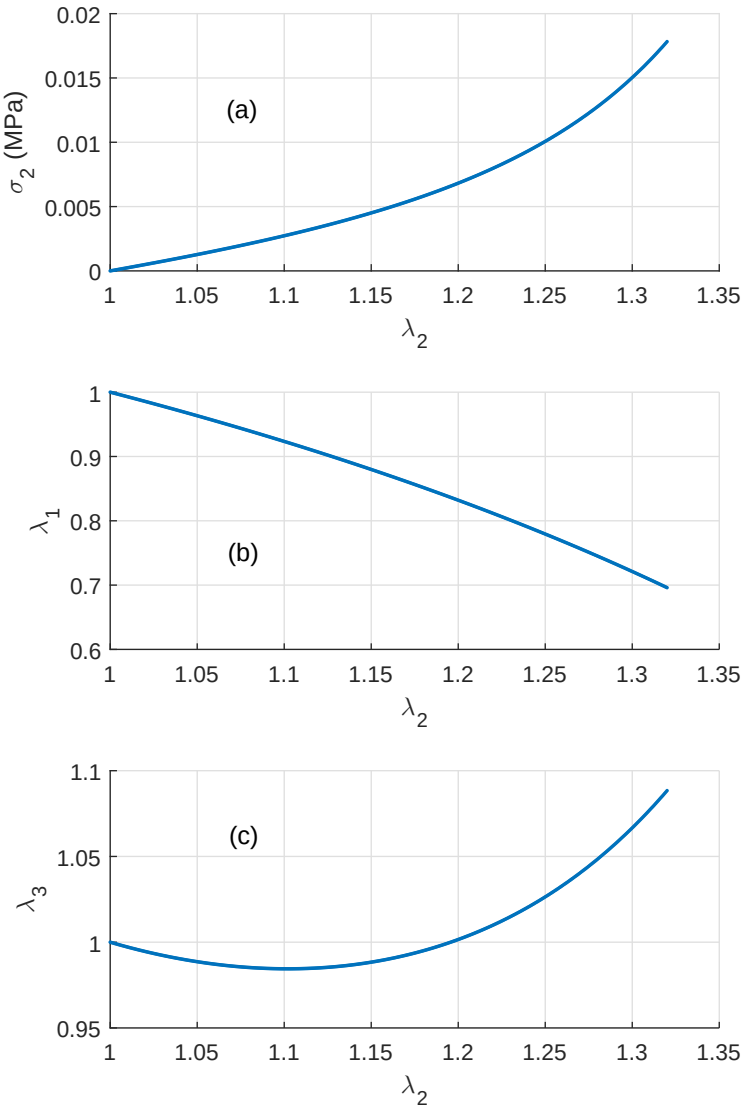

Figure 3: Uniaxial test over the circumferential specimen (direction 2 in Figure 1) using the model of Section 2. (a) Uniaxial stress in circumferential direction σ_2 (b) Transverse stretch in axial direction λ_1 (c) Transverse stretch in radial direction λ_3.

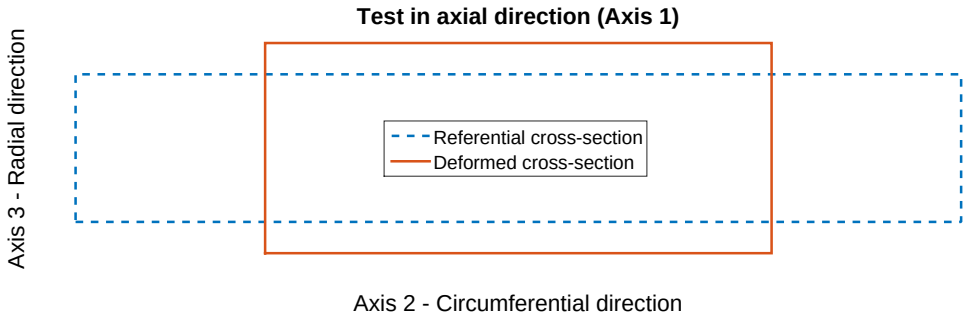

Figure 4: Undeformed and deformed ($\lambda_1 = 1.228$) cross-sectional areas of the stretched axial specimen using the model of Section 2.

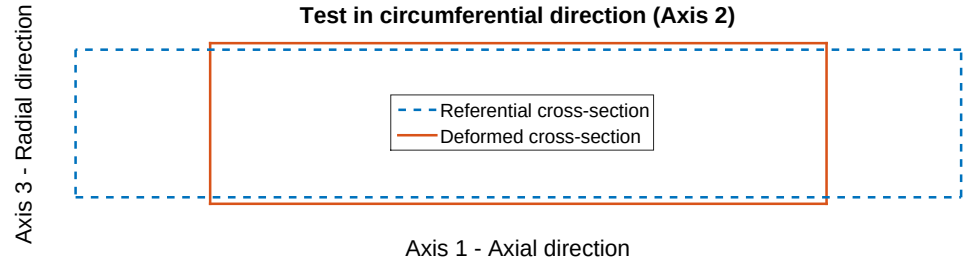

Figure 5: Undeformed and deformed ($\lambda_2 = 1.32$) cross-sectional areas of the stretched circumferential specimen using the model of Section 2.

deformation pattern was already identified by Gasser et al. in Ref. [23], see Figure 9 therein. For further comparison, we show in Figures 4 and 5 the undeformed and deformed cross-sections of both specimens. The deformed configurations in Figures 4 and 5 correspond to the maximum uniaxial stretches shown in Figures 2 ($\lambda_1 = 1.228$) and 3 ($\lambda_2 = 1.32$), respectively. We clearly observe the increment of thickness (extension in radial direction 3) in both cases. We note that this type of behavior is not usually encountered in composite linear materials [1]. As mentioned, those strains may be very relevant in 3D or constrained 2D analyses, where the boundary conditions over the third direction may greatly influence the in-plane behavior. At this point we emphasize that it is important to capture the complete in-axes behavior of the orthotropic material, not just two curves, if a general (not just uniaxial) analysis is to be performed.

3. Gasser–Ogden–Holzapfel fiber dispersion model

The unrealistic transverse deformation behavior obtained with the model of the preceding section is a direct consequence of the fact that the mechanical response of the tissue perpendicular to the fibers is mostly dominated by the soft groundmatrix for this (idealized) model with aligned fibers [23]. A more realistic behavior in terms of transverse deformations is obtained if the previous model is modified in order to take into account the fiber dispersion within the tissue, so the overall stiffness in radial direction is somewhat increased. As a result, large extensions in that direction are prevented. A model of this type is presented in Ref. [23]. Moreover, with this modification, the model becomes well-suited to describe the experimentally observed stiffening of adventitial strips, which is not predicted by the model with aligned fibers within the typical range of deformation, in general.

The fiber dispersion model introduced by Gasser, Ogden and Holzapfel in Ref. [23] is based on the Generalized Structure Tensor (GST) approach. This GST hyperelastic formulation modifies the argument of the free-energy fiber family functions $\mathcal{W}_{fi}$ of Eq. (2) as

$$\mathcal{W}_{fi}(\bar{A}_i) = \mathcal{W}_f(\bar{A}_i) = \frac{k_1}{2k_2}\left[\exp\left(k_2\bar{A}_i^2\right) - 1\right] \tag{8}$$

where the so-called structure invariant $\bar{A}_i$ represents an averaged Green–Lagrange strain measure relative to the ith dispersed fiber family defined through [28] —this invariant is usually represented as $\bar{E}_i$, but we use below the symbol E for logarithmic strains

$$\bar{A}_i = \boldsymbol{H}_i : (\bar{\boldsymbol{C}} - \boldsymbol{I}) = \boldsymbol{H}_i : \bar{\boldsymbol{C}} - \operatorname{tr} \boldsymbol{H}_i \tag{9}$$

where

$$\boldsymbol{H}_i = \kappa \boldsymbol{I} + (1 - 3\kappa)\, \boldsymbol{a}_{0i} \otimes \boldsymbol{a}_{0i} \tag{10}$$

is the ith Generalized Structure Tensor and κ the dispersion (structural) parameter. The second-order tensor $\boldsymbol{H}_i$ characterizes the fiber dispersion effects about the main orientation $\boldsymbol{a}_{0i}$ through a weighted combination of a fully isotropic (spherical) distribution of fibers and a perfectly aligned distribution of fibers. For more details about how this model is motivated and built from pre-integration of the specific fiber family distribution, the reader is referred to Ref. [23]. Other more elaborated structure-tensor-based approaches can be seen in Refs. [28], [38], [54] and [55].

For the GOH-GST model, Eq. (9) is expressed in terms of κ, $\bar{I}_1$ and $\bar{I}_{4i}$ as $\bar{A}_i = \kappa(\bar{I}_1 - 3) + (1 - 3\kappa)\,(\bar{I}_{4i} - 1)$. Note that for $\kappa = 0$ the model reduces to the model with perfectly aligned fibers described in Section 2, i.e. $\mathcal{W}_f(\bar{A}_i) \equiv \mathcal{W}_f(\bar{I}_{4i} - 1)$.

On the other hand, the value $\kappa = 1/3$ is associated to the case with isotropically distributed fibers, for which $\boldsymbol{H}_i \equiv \frac{1}{3}\boldsymbol{I}$ and $\bar{A}_i \equiv \bar{I}_1/3 - 1$, so each fiber family contribution $\mathcal{W}_f(\bar{A}_i) \equiv \mathcal{W}_f(\bar{I}_1/3 - 1)$ becomes isotropic in the limit.

3.1. Uniaxial testing

The modified second Piola–Kirchhoff stresses $\bar{\boldsymbol{S}} = 2\partial\mathcal{W}/\partial\bar{\boldsymbol{C}}$ in the uniaxial tensile tests under study specialize in this case to

$$\bar{\boldsymbol{S}} = 2\frac{\partial\mathcal{W}_g}{\partial\bar{I}_1}\frac{\partial\bar{I}_1}{\partial\bar{\boldsymbol{C}}} + \sum_{i=1}^{2} 2\frac{\partial\mathcal{W}_f}{\partial\bar{A}_i}\frac{\partial\bar{A}_i}{\partial\bar{\boldsymbol{C}}} = \left[c + 4k_1\bar{A}\exp\left(k_2\bar{A}^2\right)\kappa\right]\boldsymbol{I} + 4k_1\bar{A}\exp\left(k_2\bar{A}^2\right)(1-3\kappa)\,\boldsymbol{A}_0 \tag{11}$$

where the invariant $\bar{A} := \bar{A}_1 = \bar{A}_2$ is given in terms of Eqs. (4) and (5) as

$$\bar{A} = \kappa(\bar{I}_1 - 3) + (1 - 3\kappa)(\bar{I}_4 - 1) \tag{12}$$

Similar equilibrium equations to Eqs. (6) and (7) are obtained in this case for the tensile test over the axial specimen, cf. Ref. [38]. The same procedure detailed in the preceding section can be followed to solve the corresponding equilibrium equations. The computed axial stress σ_1 and circumferential stretch λ_2, along with the radial stretch λ_3, are shown in Figure 6 for the interval $\lambda_1 \in [0, 1.228]$. The solution being shown corresponds to the value of $\kappa = 0.226$, specifically taken from Ref. [23]. Interestingly, it can be observed in Figure 6.*c* that, even including some amount of fiber dispersion in the model, there are some deformation states for which $\lambda_3 > 1$, so the thickness of the arterial wall increases with respect to its referential value. We observe, however, that the tendency of the curves $\lambda_3(\lambda_1)$ is very different for the cases $\kappa = 0$ (Figure 2.*c*) and $\kappa = 0.226$ (Figure 6.*c*) in the shown interval: the former is greater than one and is still increasing at $\lambda_1 = 1.228$, whereas the latter is also greater than one at that deformation level but is decreasing. The radial deformation in the latter case goes through a maximum and approaches to a point such that $\lambda_3 = 1$, i.e. it goes through an *inversion* point and approaches to a *perversion* point, see [56, 57] for terminology. The fact that the extension in radial direction is reduced for the case $\kappa = 0.226$ with respect to the case $\kappa = 0$ was already noticed in Ref. [23], see Figure 12 therein, even though it was not numerically quantified. We note that the invariant $\bar{I}_4$ is always greater than one in this case, see Figure 4 of Ref. [38], hence the main fiber direction is always in extension during the test.

The results regarding the uniaxial test over the circumferential strip (Axis 2 in Figure 1, $\lambda_2 \geq 1$) are shown in Figure 7. Again, the maximum extension in radial direction is reduced with respect to the case with aligned fibers, see Figure 3.*c*, even

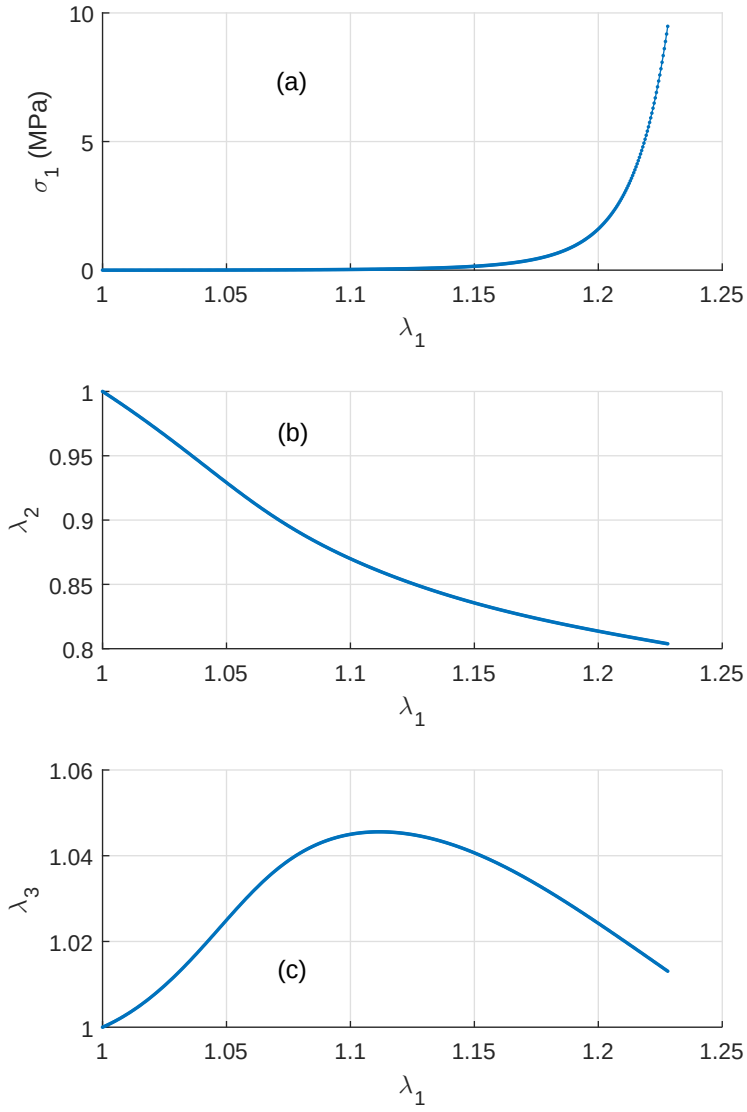

Figure 6: Uniaxial test over the axial specimen (direction 1 in Figure 1) using the model of Section 3. (a) Uniaxial stress in axial direction σ_1 (b) Transverse stretch in circumferential direction λ_2 (c) Transverse stretch in radial direction λ_3.

though the transverse deformation $\lambda_3\,(\lambda_2)$ is greater than one for some deformation states. It is important to remark that in this case the invariant $\bar{I}_4$ is lower or equal than one within the interval $1.0132 \lessapprox \lambda_2 \lessapprox 1.256$, cf. Ref. [38], so some mechanism to exclude the contribution of the contracted fibers in the given potential should have been applied if the common assumption that fibers do not support compression is accepted. The tension-compression switch to be applied should be smooth enough in order to give both continuous stresses and equilibrated and compatible (hyperelastic) solutions within the typical ranges of deformation. We refer to Ref. [38] for a recent, physically motivated proposal. However, this is not relevant for the present analysis regarding transverse deformation effects. We note that the main fiber orientations are extended, i.e. $\bar{I}_4 > 1$, when $\lambda_2 = 1.32$ and the radial deformation is positive $\lambda_3\,(\lambda_2 = 1.32) > 1$, see Figure 7. Hence the hyperelastic solution at $\lambda_2 = 1.32$ is compatible with the switch criterion proposed by the authors in Ref. [23].

We can effectively observe in Figures 8 and 9 that the increment of thickness of the axial (at $\lambda_1 = 1.228$) and circumferential (at $\lambda_2 = 1.32$) specimens is reduced, and somehow controlled, when they are compared to those of the respective deformed configurations of Figures 4 and 5. However, in our opinion, the radial deformation patterns *given* by this model, as shown in Figures 6.*c* and 7.*c*, are still unrealistic and have not been verified against experimental evidence. Indeed, we show in the next section that the transverse deformation of an incompressible orthotropic material should be material-dependent (i.e. given by experiments) and not model-dependent (i.e. given by the model as a result). Then, a given material model should be able to describe this experimental evidence. A recent analysis [57] shows the relevance of the the expansion and contraction in transverse direction *given* by certain models under uniaxial testing in assessing their applicability to fiber-reinforced materials. As it occurs within the corresponding small strains regime, the transverse deformation should not be left to be *given* by the model, unless the model prediction is verified against experiments. Indeed, the model with aligned fibers may represent the overall material behavior in some cases, as in [32], but in other cases the predictions will be inconsistent with the experimental observations, as shown in [37].

4. Spline-based model of Latorre and Montáns

The models presented in the previous sections depend, in essence, on the three invariants $\bar{I}_1$, $\bar{I}_{41}$ and $\bar{I}_{42}$. Other more recent structure tensor formulations, e.g. [54, 55], use strain energy functions depending on the same invariants, even though including higher order terms of the Taylor expansion of the anisotropic strain energy contribution. Anisotropic hyperelastic models based on the three invariants $\bar{I}_1$, $\bar{I}_{41}$

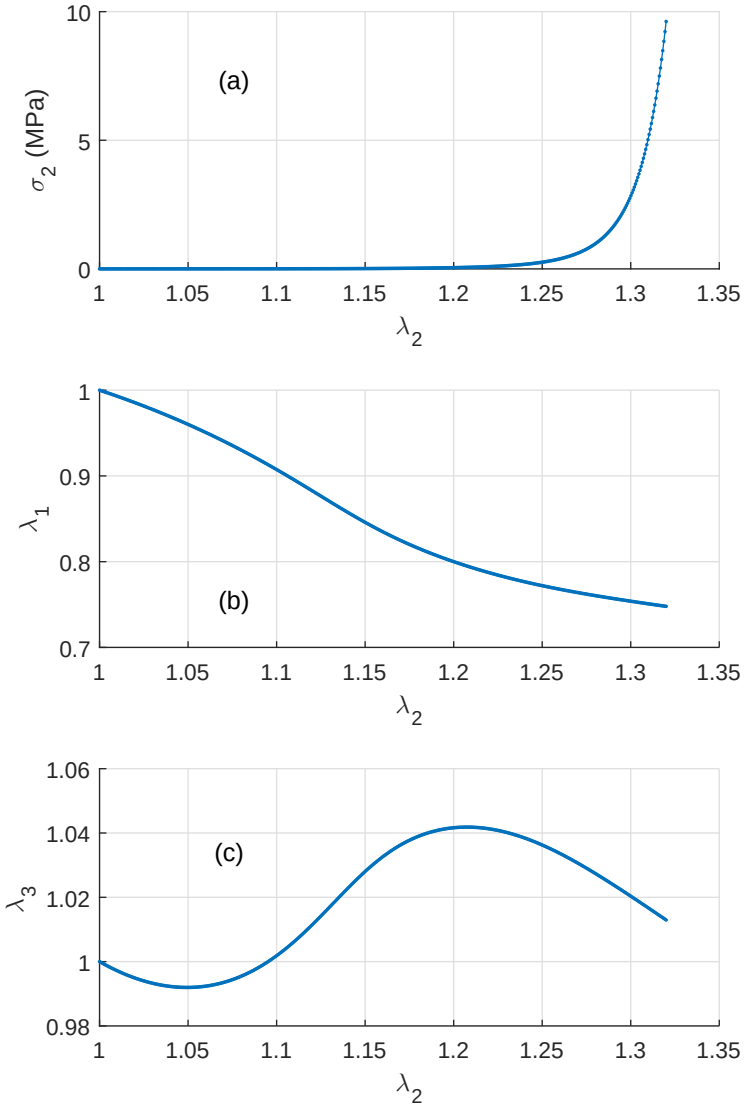

Figure 7: Uniaxial test over the circumferential specimen (direction 2 in Figure 1) using the model of Section 3. (a) Uniaxial stress in circumferential direction σ_2 (b) Transverse stretch in axial direction λ_1 (c) Transverse stretch in radial direction λ_3.

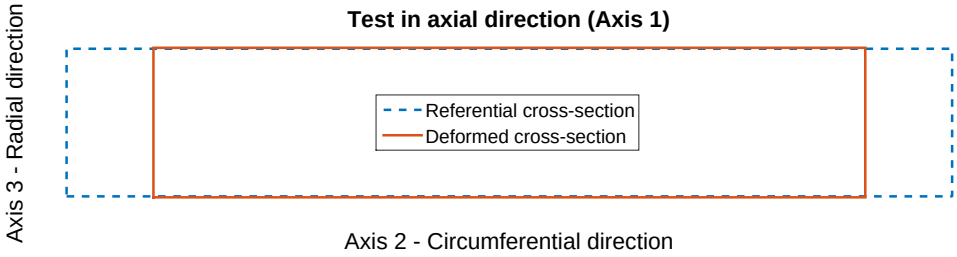

Figure 8: Undeformed and deformed ($\lambda_1 = 1.228$) cross-sectional areas of the stretched axial specimen using the model of Section 3.

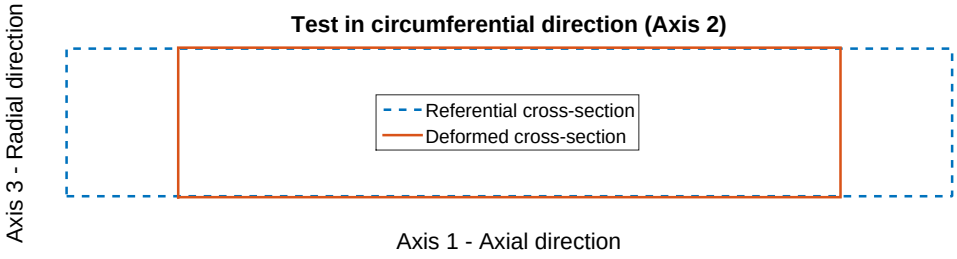

Figure 9: Undeformed and deformed ($\lambda_2 = 1.32$) cross-sectional areas of the stretched circumferential specimen using the model of Section 3.

and $\bar{I}_{42}$ are frequently determined fitting experimental data from uniaxial tensile tests over circumferential and axial arterial specimens alone [23]. As we show below, only with these experimental curves it is not possible, in general, to reproduce the actual finite strain behavior of an orthotropic material along preferred axes and, by no way, to reproduce the shear behavior in preferred planes. Furthermore, the optimization procedure used to determine the material parameters of these models may lead to obtain anisotropic material parameters when the experimental data corresponds to an isotropic material in the limit [34]. Another consequence regarding simplified strain energies of this type is that they do not reproduce the behavior of the arterial wall (or any other real material) in the infinitesimal deformation case [35].

The spline-based orthotropic model of Ref. [44] overcomes the three preceding drawbacks just pointed out. That is, we show below that it is capable to exactly and completely reproduce the finite strain responses of the arterial wall about preferred directions (this being its most appealing feature and, in practice, the most relevant one) and that it is fully consistent with the linear theory by construction; being also easily re-formulated to achieve both theoretical and numerical material-symmetries congruency [34]. The model in Ref. [44] is formulated in terms of separate functions ω_{ij} of the six components of the deviatoric logarithmic strain tensor $\bar{\boldsymbol{E}} = \frac{1}{2}\ln \bar{\boldsymbol{C}}$ in the orthotropic preferred basis $X_{pr} = \{\boldsymbol{e}_1, \boldsymbol{e}_2, \boldsymbol{e}_3\}$ of the material under study as

$$\mathcal{W} = \sum_{i,j=1}^{3} \omega_{ij}(\bar{E}_{ij}) \tag{13}$$

This strain energy function depends on the six invariants $\bar{E}_{ij} = \boldsymbol{e}_i \cdot \bar{\boldsymbol{E}} \boldsymbol{e}_j$, from which only five are independent due to the incompressibility constraint $\bar{E}_{11} + \bar{E}_{22} + \bar{E}_{33} = 0$.

4.1. Consistency with the infinitesimal behavior

Certainly, as emphatized in Ref. [35], consistency with the linear theory should be an essential feature of any nonlinear model. In this case, the correct limit is simply attained if —compare to the complex conditions to be satisfied by models based on Cauchy–Green invariants and pseudo-invariants $\bar{I}_i$ given in [35]

$$\left.\frac{\partial^2 \mathcal{W}}{\partial \bar{E}_{ij}^2}\right|_{\bar{E}_{ij}=0} = \left.\frac{\partial^2 \omega_{ij}(\bar{E}_{ij})}{\partial \bar{E}_{ij}^2}\right|_{\bar{E}_{ij}=0} = 2\mu_{ij} \tag{14}$$

where μ_{ij} are the six reference deviatoric (shear-like) moduli that completely define the incompressible orthotropic behavior within the infinitesimal context. Then, the

linearized strain energy function reads

$$\mathcal{W}_{lin} = \sum_{i,j=1}^{3} \mu_{ij} \bar{E}_{ij}^2 \equiv \sum_{i,j=1}^{3} \mu_{ij} \bar{\varepsilon}_{ij}^2 \tag{15}$$

where $\bar{\varepsilon}_{ij}$ are the components of the infinitesimal deviatoric strain tensor in the material orthotropy basis X_{pr}.

4.2. Explicit determination of the linear model

The main aim of this Section is to derive some explicit results from the linear/linearized model of Eq. (15) that will prove useful for the implicit determination procedure of the nonlinear finite strain model of Eq. (13). At the same time, we also illustrate the consequences of overlooking transverse deformation effects in uniaxial tests. The raised conclusions will be evidently applicable to the more general, large strain context.

Six experimental curves (straight lines or slopes, indeed) are required to completely determine the infinitesimal (or linearized) model given in Eq. (15). This is usually done by means of three experimental *curves* obtained from uniaxial testing along the preferred directions, from which we can determine μ_{11}, μ_{22} and μ_{33}, and other three experimental *curves* obtained from shear tests within the preferred planes of symmetry, that directly give the shear moduli $\mu_{12} = G_{12}$, $\mu_{23} = G_{23}$ and $\mu_{31} = G_{31}$. The deviatoric moduli μ_{11}, μ_{22} and μ_{33} can be related to the more usual Young's moduli Y_1 and Y_2 and the Poisson ratio ν_{12} through [39] —we use the symbol Y for Young's moduli instead of E in order to avoid confusion with logarithmic strains

$$Y_1 = 2\frac{\mu_{11}\mu_{22} + \mu_{22}\mu_{33} + \mu_{33}\mu_{11}}{\mu_{22} + \mu_{33}} \tag{16}$$

$$Y_2 = 2\frac{\mu_{11}\mu_{22} + \mu_{22}\mu_{33} + \mu_{33}\mu_{11}}{\mu_{33} + \mu_{11}} \tag{17}$$

$$\nu_{12} = \frac{\mu_{33}}{\mu_{22} + \mu_{33}} \tag{18}$$

It should be apparent now that three independent experimental curves (with slopes Y_1, Y_2 and ν_{12}, or any other combination of independent Young's moduli and Poisson's ratios) are needed to properly characterize the linear in-axes behavior of an incompressible orthotropic material. If we only know the Young's moduli Y_1 and Y_2, then there exist infinite (mathematical) solutions $\{\mu_{11}, \mu_{22}, \mu_{33}\}$ that fulfill Eqs. (16) and (17). Subsequently, each one of these "solutions" will predict a different Poisson

ratio ν_{12} using Eq. (18) as a result. Evidently, only one of those (mathematical) solutions will be the correct (physical) solution that reproduces the material behavior for small strains. We will show this fact in the example below in the context of finite strains.

As mentioned, we have just explained this very simple linear example to describe what may be happening when the nonlinear models of the previous sections (or other similar models) are determined from two uniaxial stress-strain curves only (i.e. two Young's moduli in the infinitesimal limit). In that case, even if we are able to exactly replicate the two non-linear stress-strain experimental curves, the transverse deformation (i.e. the Poisson ratio) is, as a result, defined by the material parameters obtained from the optimization procedure, which we note, are usually not unique and strongly dependent on the initial optimization parameters. In other words, *the transverse deformation is defined by the material model* in those cases. Moreover, different local minima of the minimization procedure will provide different transverse deformation patterns. Certainly, as it occurs within the linear framework, it should be required that *the orthotropic material model is defined by the material transverse deformation* in those cases.

4.3. Nonlinear finite strain model

The model given in Eq. (13) represents the non-linear extension of the deviatoric infinitesimal model of Eq. (15) to the context of finite deformations using logarithmic strains. This extension is motivated by the fact that the logarithmic strain tensor represents a natural generalization of the infinitesimal strain tensor to the finite deformation setting [47]. In Ref. [44] we provide two different procedures to determine the first-derivative spline-based functions of the axial terms ω_{11}, ω_{22} and ω_{33} present in Eq. (13). The first one of them (Table 1 in Ref. [44]) requires as input the experimental data $\tilde{\sigma}_{11}^{(1)}(\tilde{E}_{11})$ and $\tilde{E}_{22}^{(1)}(\tilde{E}_{11})$ obtained from uniaxial tension and compression tests in direction $\boldsymbol{e}_1$ –hence the superscript (1)– and the stress-strain data $\tilde{\sigma}_{22}^{(2)}(\tilde{E}_{22})$ from uniaxial tension and compression tests in direction $\boldsymbol{e}_2$ —compare to the left-hand sides of Eqs. (16)-(18). Other possibility is to obtain the axial strain energy terms from the experimental data set $\tilde{\sigma}_{11}^{(1)}(\tilde{E}_{11})$, $\tilde{\sigma}_{22}^{(2)}(\tilde{E}_{22})$ and $\tilde{\sigma}_{33}^{(3)}(\tilde{E}_{33})$ (Table 2 in Ref. [44]). Unlike the linear case, the non-linear equilibrium equations resulting from the corresponding tests cannot be solved explicitly. Hence, two optimization procedures were proposed to solve the equilibrium equations in a least-squares sense in Ref. [44]. The unknown variables are equivalent Poisson ratios in the logarithmic strain space (with a clear physical meaning), which facilitate the initialization of the iterative procedure and the interpretation of the solution parameters. The use

of the so-called inversion formula within the procedure gives a final solution which reproduces the experimental data with a very good (exact, in practice) agreement.

The inversion formula, originally proposed by Kearsley and Zapas [59], gives an *exact* solution of the uniaxial equilibrium equation in the isotropic case. Sussman and Bathe [45] solved this equation using piecewise spline representations of both the experimental data and the first derivative function of the isotropic strain energy term ω. In Ref. [42] a compacted, more general version of the inversion formula was derived, which made possible its use with experimental data from anisotropic materials. Following this line, in the next subsection we detail an enhanced algorithmic iterative procedure (with respect to that of Table 1 in Ref. [44]) that provides the *exact* solution (close to machine precision) for the axial terms ω'_{11}, ω'_{22} and ω'_{33} when the available experimental data are the distributions $\tilde{\sigma}^{(1)}_{11}(\tilde{E}_{11})$, $\tilde{E}^{(1)}_{22}(\tilde{E}_{11})$ and $\tilde{\sigma}^{(2)}_{22}(\tilde{E}_{22})$. In this case, we need neither to invoke any optimization procedure nor to propose any specific shape (linear, exponential, etc.) for the remaining transverse strain functions present in the equilibrium equations. From now on, since we are considering the perfectly incompresible case, for which $\boldsymbol{E} = \bar{\boldsymbol{E}}$, we remove the bar decoration over the logarithmic strains for the matter of notation simplicity.

4.3.1. Implicit determination of $\omega'_{11}(E_{11})$, $\omega'_{22}(E_{22})$ and $\omega'_{33}(E_{33})$ from $\tilde{\sigma}^{(1)}_{11}(\tilde{E}_{11})$, $\tilde{E}^{(1)}_{22}(\tilde{E}_{11})$ and $\tilde{\sigma}^{(2)}_{22}(\tilde{E}_{22})$

The following algorithmic iterative procedure exactly solves (from a numerical viewpoint) the equilibrium Eqs. (70)-(74) of Ref. [44]. This is possible due to the use of continuous spline interpolations of stress-strain curves, transverse strain curves and first derivative functions of strain energy terms. Once a solution has been obtained, the model exactly replicates the axial behavior of the orthotropic material about its preferred directions. Note the difference with the procedure detailed in Table 1 of Ref. [44], where some transverse-to-axial relations were considered linear. The procedure of Table 2 in Ref. [44] can be analogously generalized.

1. Spline-based smooth continuous functions $\sigma^{(1)}_{11}(E_{11})$, $E^{(1)}_{22}(E_{11})$ and $\sigma^{(2)}_{22}(E_{22})$ are obtained from the interpolation of the tension-compression experimental data points (experimental noise should be previously removed from data). These spline-based functions, say $f_i(x)$, have to satisfy the requirements $f_i(0) = 0$. The slopes at the origin of these curves are, respectively Y_1, ν_{12} and Y_2.
2. Take the linearized relations for transverse strains as $E^{(2)}_{11}(E_{22}) = -\nu_{21}E_{22}$ and $E^{(3)}_{11}(E_{33}) = -\nu_{31}E_{33}$, associated to the corresponding orthotropic infinitesimal behavior, just to initialize the iterative procedure (iteration $k = 0$). The initial

Poisson ratios ν_{21} and ν_{31} are given from the linear theory as in [1]

$$\nu_{21} = \nu_{12}\frac{Y_2}{Y_1} \tag{19}$$

$$\nu_{31} = \frac{(1-\nu_{12})Y_2}{(1-\nu_{21})Y_1 + (1-\nu_{12})Y_2} \tag{20}$$

where

$$Y_1 = \left.\frac{d\sigma_{11}^{(1)}}{dE_{11}}\right|_{E_{11}=0}, \quad Y_2 = \left.\frac{d\sigma_{22}^{(2)}}{dE_{22}}\right|_{E_{22}=0} \quad \text{and} \quad \nu_{12} = -\left.\frac{dE_{22}^{(1)}}{dE_{11}}\right|_{E_{11}=0} \tag{21}$$

3. Compute the initial ($k = 0$) spline-based functions $\omega'_{11}(E_{11})$, $\omega'_{22}(E_{22})$ and $\omega'_{33}(E_{33})$ associated to the initial transverse distributions $E_{11}^{(2)}(E_{22})$ and $E_{11}^{(3)}(E_{33})$ following steps 5 to 7 in Table 1 of Ref. [44].
4. Update the first derivative function of $E_{11}^{(2)}(E_{22})$ and $E_{11}^{(3)}(E_{33})$ at iteration $k+1$ through

$$\left.\frac{dE_{11}^{(2)}(E_{22})}{dE_{22}}\right|_{k+1} = -\left.\frac{\omega''_{33}\left(E_{33}^{(2)}(E_{22})\right)}{\omega''_{11}\left(E_{11}^{(2)}(E_{22})\right) + \omega''_{33}\left(E_{33}^{(2)}(E_{22})\right)}\right|_{k} \tag{22}$$

$$\left.\frac{dE_{11}^{(3)}(E_{33})}{dE_{33}}\right|_{k+1} = -\left.\frac{\omega''_{22}\left(E_{22}^{(3)}(E_{33})\right)}{\omega''_{11}\left(E_{11}^{(3)}(E_{33})\right) + \omega''_{22}\left(E_{22}^{(3)}(E_{33})\right)}\right|_{k} \tag{23}$$

   which are obtained after differentiating Eqs. (73) and (74) in Ref. [44] and considering the respective incompressibility constraints. Remarkably, note that Eqs. (22) and (23) are the non-linear counterpart of the small strains Poisson's ratios expressed in terms of the deviatoric moduli –cf. Eq. (18) above or the general Expression (140) in Ref. [39].
5. Build the piecewise cubic splines $\left(E_{22}, dE_{11}^{(2)}(E_{22})/dE_{22}\right)_{k+1}$ and $\left(E_{33}, dE_{11}^{(3)}(E_{33})/dE_{33}\right)_{k+1}$. Note that for these functions, say $g_j(x)$, the requirements $g_j(0) = 0$ do not have to be enforced.
6. Integrate the first-derivative functions of step 5 and then build the updated splines $E_{11}^{(2)}(E_{22})$ and $E_{11}^{(3)}(E_{33})$ at iteration $k+1$. At this step, consider the (integration) requirements $E_{11}^{(j)}(0) = 0$.
7. Compute the updated spline-based functions $\omega'_{11}(E_{11})$, $\omega'_{22}(E_{22})$ and $\omega'_{33}(E_{33})$

following steps 5 to 7 in Table 1 of Ref. [44].

8. Quantify the associated relative error for the transverse strains set $[E_{11}^{(2)}(E_{22}), E_{11}^{(3)}(E_{33})]$ between iterations k and $k+1$. Exit if $error \leq tolerance$. Take $k \leftarrow k+1$ and go to step 4 if $error > tolerance$.

Note that this is a self-contained iterative procedure in which the required data to be initialized are contained in the experimental data of Step 1. In other words, we do not need to propose specific numerical values from which start the iterations. For all the examples shown below, which include the typical strong non-linearities of biological tissues, the present procedure has converged in few iterations ($k \approx 25$) to the numerically exact solution ($tolerance = 10^{-14}$) using these self-contained, initial values. Note that this is a extremely small *tolerance* value close to the machine precision. Indeed, for all the cases being analyzed below, the stress and transverse strain predictions become practically indistinguishable for $tolerance = 10^{-3}$, which is a tolerance for transverse strains we typically enforce.

The fact that we solve the equilibrium equations in an exact way (instead of solving it in a least-squares sense), and without needing to propose guess values, represents a clear advantage of this procedure with respect to the non-linear least squares optimization methods frequently used to determine hyperelastic functions with an initially assumed analytical shape. See for example Ref. [33] for inherent difficulties associated to this type of optimization procedures even for the simpler case of isotropic material models. Obviously, for anisotropic material models the situation is even worse [60], [19]. We provide some insight into this issue in Ref. [52] regarding uniaxial and biaxial *tensile* tests.

4.4. Uniaxial testing: capturing transverse deformation effects in arteries

In this section we use the model of Eq. (13) and apply the procedure of Section 4.3.1 in order to exactly replicate the uniaxial stresses predicted by the fiber dispersion model of Gasser et al. [23] for advential tissue. That is, we consider the stresses of Figures 6.*a* and 7.*a* as the "experimental" stresses $\sigma_{11}^{(1)}(E_{11})$ and $\sigma_{22}^{(2)}(E_{22})$ in the step 1 of Section 4.3.1. Note that in the calculations of Figure 7 we have not considered any tension-compression switch in order to exclude the contribution of fibers in compression. However, we could equally use the stresses predicted by this model along with the consideration of a given continuous criterion [38] as the "experimental" data $\sigma_{22}^{(2)}(E_{22})$. In this case, the response of the arterial layer with compressed fibers excluded would be included in the stress-strain experimental data $\sigma_{22}^{(2)}(E_{22})$ and the phenomenological model of Eq. (13) would also include that information. Note also that the shear terms in Eq. (13) are irrelevant for the present in-axes study. The

shear terms in Eq. (13) are to be obtained from three additional shear tests in the corresponding preferred planes. If these experimental data are not available at large strains, then an extrapolation using both logarithmic strains and the infinitesimal shear moduli, see Eq. (15), may be assumed and prescribed by the user in order to use the model of Eq. (13) in more generic off-axes responses. In an equivalent way to what occurs for the transverse deformation in the in-axes behavior, we advocate prescribing a realistic shear behavior (which, in essence, is material-dependent for orthotropic materials) rather than let the model further predict a likely unrealistic shear behavior (i.e. model-dependent).

The main point of this example is that we exactly reproduce both highly nonlinear stress responses of Figures 6.*a* and 7.*a* for several "experimental" transverse strains curves $E_{22}^{(1)}(E_{11})$ being additionally prescribed at step 1 of Section 4.3.1. On the other hand, the beauty of this academic example is that we will be able to interpret all the obtained finite strain results analogously as we would do within the infinitesimal strains framework. In that respect, and without loss of generality, we take the stiffest direction of the tissue (in axial direction) as direction 1 of our model, recall Figure 1, which will let us explain the orthotropic behavior more easily.

We next show the results obtained when we consider as initial data the "experimental" linear transverse strains $E_{22}^{(1)} = -\nu_{12}E_{11}$ in the procedure of Section 4.3.1 along with the "experimental" stress responses $\sigma_{11}^{(1)}(E_{11})$ and $\sigma_{22}^{(2)}(E_{22})$. We compute five different sets of strain energy axial terms $\omega'_{11}(E_{11})$, $\omega'_{22}(E_{22})$ and $\omega'_{33}(E_{33})$ for five different in-plane equivalent Poisson ratios $\nu_{12} = \{0.1, 0.2, 0.3, 0.4, 0.5\}$.

In Figure 10 we show the stresses predicted by the model for each value ν_{12}. We can see in the left figure that the "experimental" stresses $\sigma_{11}^{(1)}(E_{11})$ and $\sigma_{22}^{(2)}(E_{22})$ are *exactly* replicated in all the cases. In the right figure, however, we see that each strain energy function being obtained predicts different uniaxial stresses $\sigma_{33}^{(3)}(E_{33})$ for a hypothetical tensile test in the radial direction 3 (cf. Eq. (83) of Ref. [44]). At this point, note the analogy of this non-linear case with the discussion above regarding the linear Relations (16)-(18). That is, there are infinite sets of axial terms of the strain energy $\omega'_{11}(E_{11})$, $\omega'_{22}(E_{22})$ and $\omega'_{33}(E_{33})$ (equivalently, μ_{11}, μ_{22} and μ_{33} for the small strains case) that *exactly* reproduce a given pair of experimental curves $\sigma_{11}^{(1)}(E_{11})$ and $\sigma_{22}^{(2)}(E_{22})$ (equivalently, Y_1 and Y_2). Hence, a third experimental, independent curve (e.g. transverse strains $E_{22}^{(1)}(E_{11})$) is strictly necessary in order to determine the specific in-axes behavior of the incompressible orthotropic material being characterized. As aforementioned, if the third in-axes behavior curve is not available from experiments, we should propose a realistic one (e.g. $E_{22}^{(1)} \simeq -\nu_{12}E_{11}$ with $0 < \nu_{12} < 0.5$, see Eq. (1) and Fig. 11.*C* in Ref. [37]) before determining the strain energy function contributions in preferred axes, as we have successfully done

in this work.

Furthermore, in Figure 10.*b* we see that the higher the value ν_{12}, the stiffer the response $\sigma_{33}^{(3)}(E_{33})$. We can explain this result considering that the higher the value ν_{12}, the larger the contraction in the circumferential direction $E_{22}^{(1)} = -\nu_{12}E_{11}$ for a fixed value E_{11}, the smaller the contraction in radial direction by incompressibility $E_{33}^{(1)} = -E_{11} - E_{22}^{(1)} = -(1-\nu_{12})E_{11}$, i.e. the higher the relative stiffness of the material in the radial direction with respect to the circumferential direction. Interestingly, the same result is analytically deduced from the small strains relation given in Eq. (18). In fact, it is obtained that the computed curve $\sigma_{33}^{(3)}(E_{33})$ predicts lower values than the prescribed curve $\sigma_{22}^{(2)}(E_{22})$ for $\nu_{12} < 0.5$ (i.e. $Y_1 > Y_2 > Y_3$) and that $\sigma_{33}^{(3)}(E_{33}) \equiv \sigma_{22}^{(2)}(E_{22})$ for $\nu_{12} = 0.5$ (i.e. $Y_1 > Y_2 = Y_3$). In this last case, it is obtained from the computations that the strain energy axial terms are also coincident, $\omega'_{22}(E_{22}) \equiv \omega'_{33}(E_{33})$, and the in-axes behavior is transversely isotropic. If, additionally to $\mu_{22} = \mu_{33}$, we obtain from the small strain behavior the relation $\mu_{23} = \mu_{22} = \mu_{33}$, then the transversely isotropic model of Refs. [42, 43], should be used (with direction 1 being the anisotropic direction).

We show in Figure 11 the different solutions $E_{11}^{(2)}(E_{22})$ y $E_{11}^{(3)}(E_{33})$ being computed for each "experimental" input distribution $E_{22}^{(1)} = -\nu_{12}E_{11}$ considered in the procedure of Section 4.3.1. For example, in Figure 11.*b* we observe that the higher the value ν_{12}, the larger the contraction $E_{11}^{(2)}(E_{22})$. We can easily explain this result focusing on the small strain Relation (19). Since the referential Young's moduli Y_1 and Y_2 are the same for all the cases under study, see Eq. (21), then the higher the value ν_{12}, the higher the value ν_{21} in Eq. (19), i.e. the larger the (non-linear) transverse contraction $E_{11}^{(2)}(E_{22})$ in the uniaxial test along the circumferential direction 2. Furthermore, since $Y_1 > Y_2$, Eq. (19) gives the small strains relation $\nu_{21} < \nu_{12}$. The same qualitative behavior is obtained for large strains, which can be verified comparing the respective finite, non-linear behaviors in Figures 11.*a* (prescribed curves) and 11.*b* (computed curves). We have also represented in Figure 11 the linear extrapolations from the small strains theory $E_{11}^{(2)}(E_{22}) = -\nu_{21}E_{22}$ and $E_{11}^{(3)}(E_{33}) = -\nu_{31}E_{33}$ (used also at step 2 of Section 4.3.1 to initialize the iterative procedures). We can see that the non-linear solution curves $E_{11}^{(2)}(E_{22})$ and $E_{11}^{(3)}(E_{33})$ approach their respective linear behavior curves in the limit of small strains, i.e. the spline-based model of Eq. (13) is fully consistent with the small strains theory, see Eq. (14).

We represent the first derivative functions $\omega'_{11}(E_{11})$, $\omega'_{22}(E_{22})$ and $\omega'_{33}(E_{33})$ being computed for each ν_{12} case in Figure 12. Although each pair of curves $\omega'_{11}(E_{11})$ and $\omega'_{22}(E_{22})$ on the left figure are almost identical for all the values ν_{12} and for finite strains, they are not exactly coincident. In particular, these subtle differences become

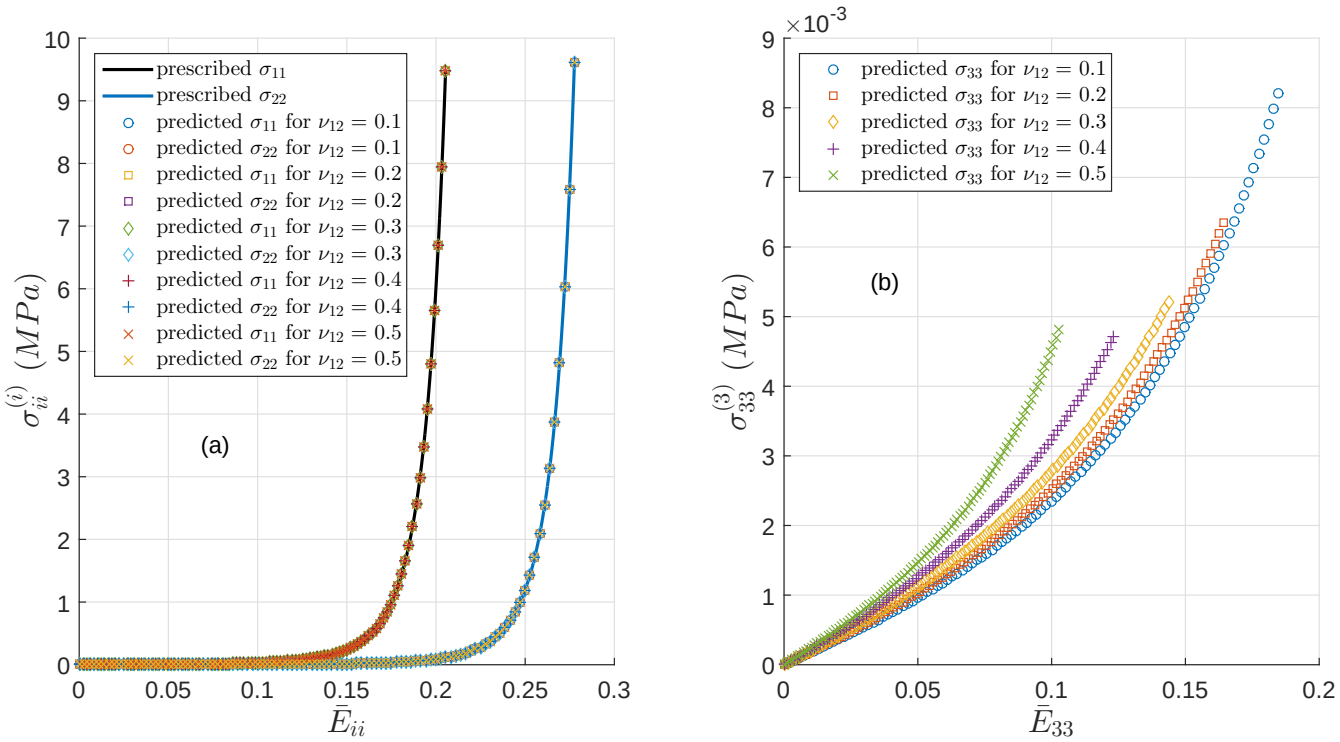

Figure 10: (a) "Experimental" stresses $\sigma_{11}^{(1)}(\bar{E}_{11})$ and $\sigma_{22}^{(2)}(\bar{E}_{22})$ and *exact* predictions using the model of Section 4 for different "experimental" prescriptions $\bar{E}_{22}^{(1)}(\bar{E}_{11}) = -\nu_{12}\bar{E}_{11}$. Due to the absence of experimental compression data, we have assumed $\sigma_{11}^{(1)}(-\bar{E}_{11}) = -\sigma_{11}^{(1)}(\bar{E}_{11})$ and $\sigma_{22}^{(2)}(-\bar{E}_{22}) = -\sigma_{22}^{(2)}(\bar{E}_{22})$ in order to apply the inversion formula [52]. (b) Model predictions $\sigma_{33}^{(3)}(\bar{E}_{33})$ in a hypothetical uniaxial test in direction 3.

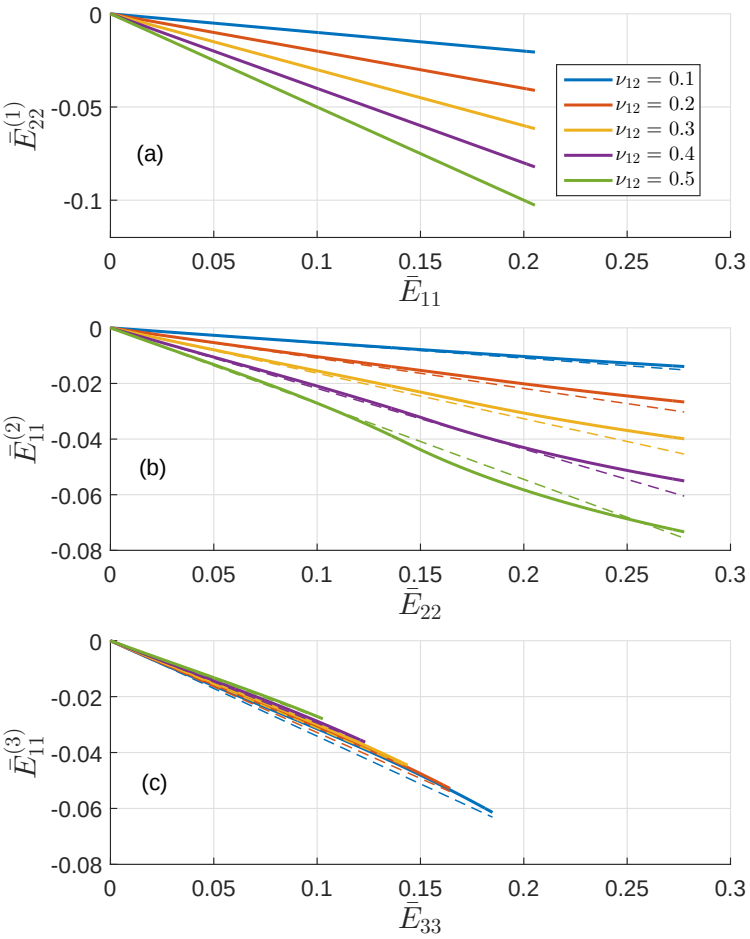

Figure 11: (a) "Experimental", prescribed transverse logarithmic strains $\bar{E}_{22}^{(1)}(\bar{E}_{11}) = -\nu_{12}\bar{E}_{11}$ (b) Corresponding computed transverse strains solutions $\bar{E}_{11}^{(2)}(\bar{E}_{22})$ (solid lines) and linear extrapolations $\bar{E}_{11}^{(2)}(\bar{E}_{22}) = -\nu_{21}\bar{E}_{22}$ using the respective small strains Poisson ratios ν_{21} (dashed lines) (c) Corresponding computed transverse strains solutions $\bar{E}_{11}^{(3)}(\bar{E}_{33})$ (solid lines) and linear extrapolations $\bar{E}_{11}^{(3)}(\bar{E}_{33}) = -\nu_{31}\bar{E}_{33}$ using the respective small strains Poisson ratios ν_{31} (dashed lines).

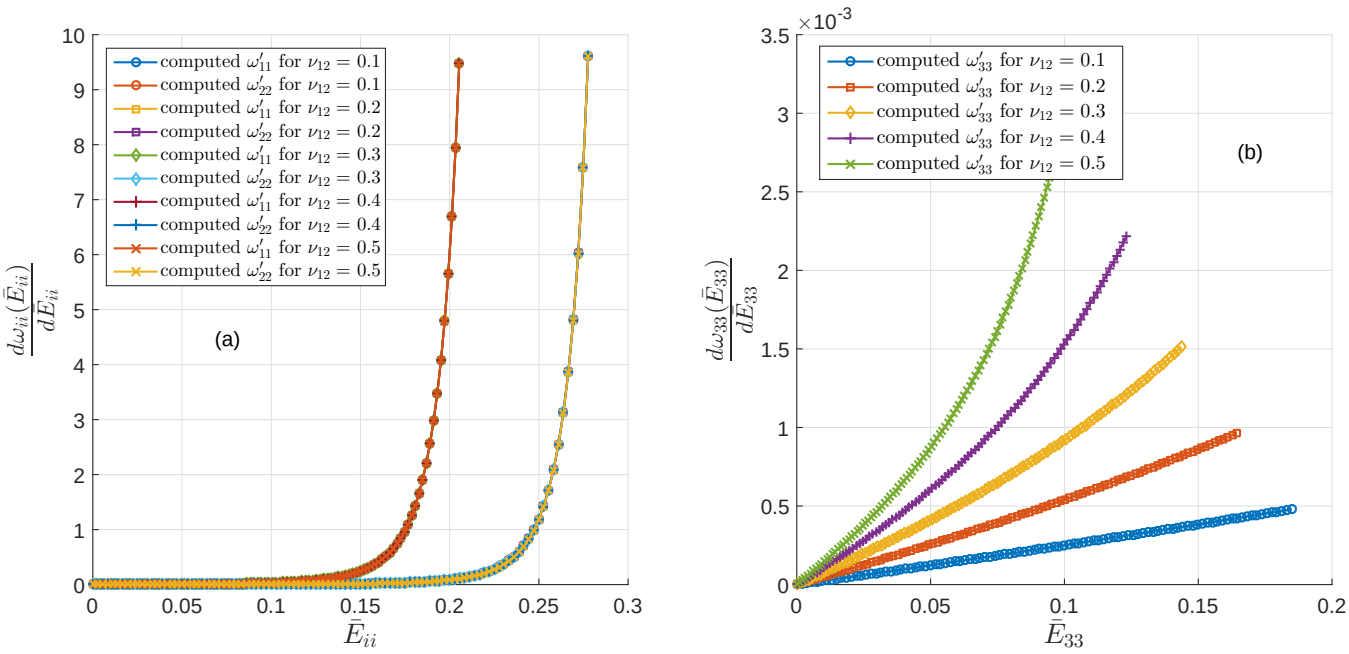

Figure 12: (a) Computed strain energy solution $\omega'_{11}(\bar{E}_{11})$, $\omega'_{22}(\bar{E}_{22})$ for different "experimental" prescriptions $\bar{E}^{(1)}_{22}(\bar{E}_{11}) = -\nu_{12}\bar{E}_{11}$. (b) Corresponding first derivative terms $\omega'_{33}(\bar{E}_{33})$. Energy units of MJ / m^3.

extremely relevant in order to attain the aforementioned consistency with the linear theory. We represent these curves, along with the stress predictions of Figure 10.*a*, within the small strains interval $\varepsilon \simeq E < 10^{-2}$ in Figure 13. Remarkably, note that the computed referential deviatoric stiffnesses, as given in Eq. (14), are different for each case and that the predicted Young's moduli, as given in Eq. (21), are the same for all the cases. It is straightforward to verify that each set of these values satisfy Eqs. (16)-(18) for the corresponding Poisson ratio ν_{12}. Furthermore, since this purely computational procedure does not give an energy function solution with an analytical shape, we encourage interested readers to verify that the evaluation of the right-hand sides of Eqs. (70) and (72) of Ref. [44], using the spline-based functions of Figures 12 and 11, exactly predict the "experimental" stress prescriptions of Figure 10.*a*.

Finally, in Figures 14 and 15 we show the deformed cross-sectional areas of the axial (at $\lambda_1 = 1.228$) and circumferential (at $\lambda_2 = 1.32$) specimens for all the cases under study. Note that the thickness of each deformed specimen in axial direc-

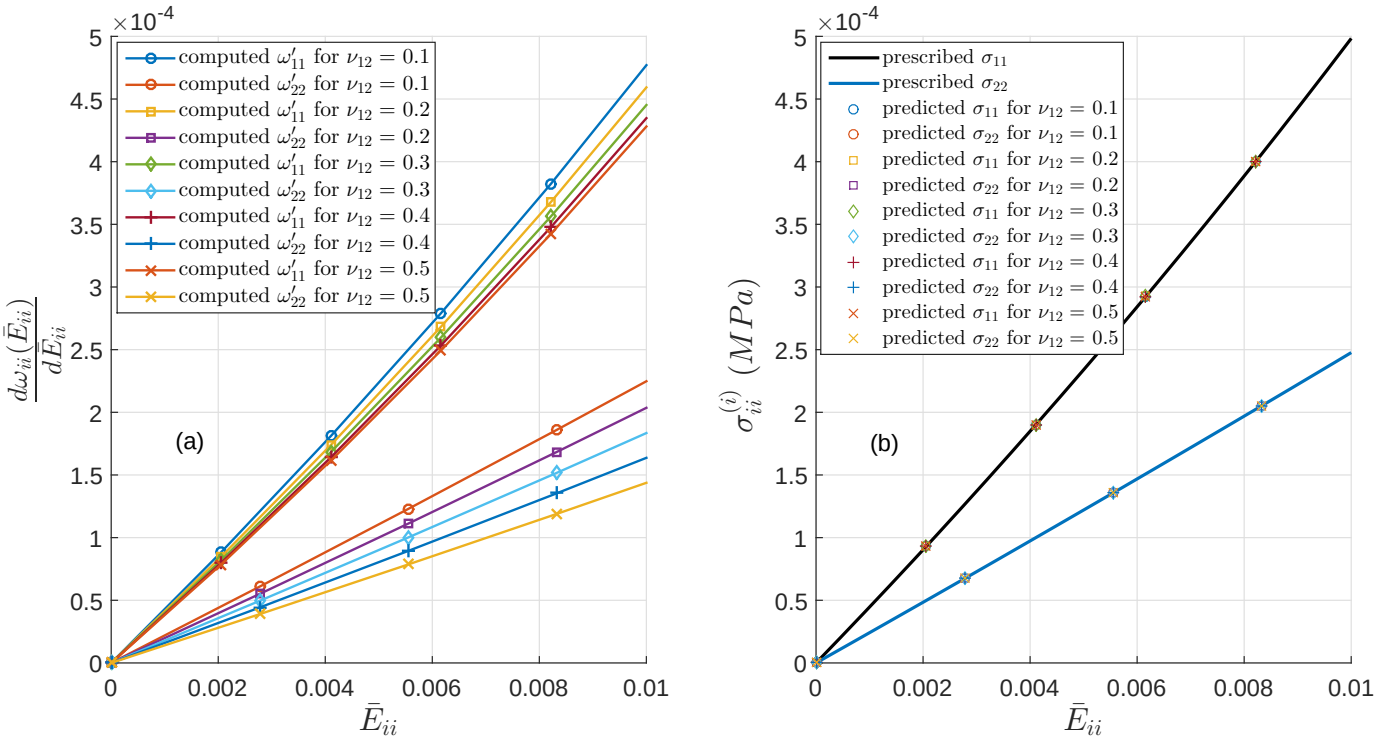

Figure 13: (a) Detail of Figure 12.a for small strains. (b) Detail of Figure 10.a for small strains.

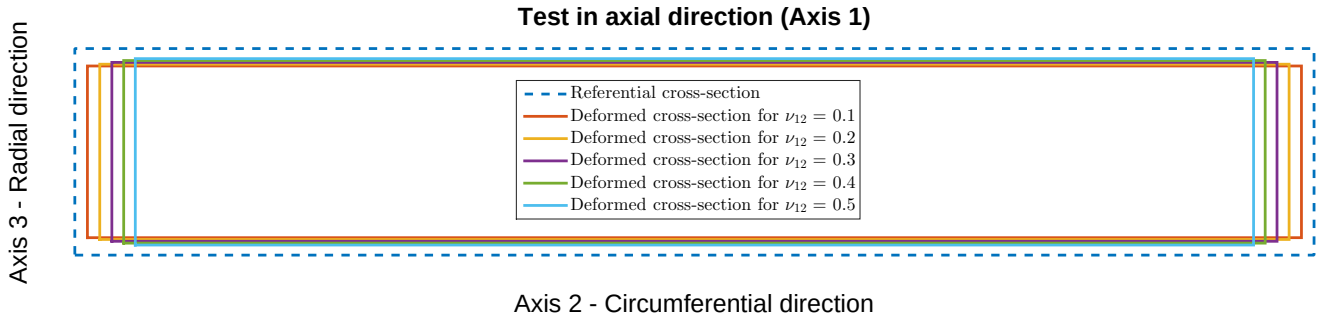

Figure 14: Undeformed and deformed ($\lambda_1 = 1.228$) cross-sectional areas of the stretched axial specimen using the model of Section 4 and different prescriptions for ν_{12}.

tion 1 is in perfect correspondence to the "experimental" value ν_{12} being prescribed in each case, i.e. the higher the value ν_{12}, the smaller the contraction in radial direction $E_{33}^{(1)} = -(1-\nu_{12})E_{11}$ for $E_{11} = \ln\lambda_1$ fixed. Certainly, this is a What-You-Prescribe-Is-What-You-Get (WYPIWYG) orthotropic hyperelastic model. The different deformations of the circumferential specimen shown in Figure 15 are also as expected beforehand. Based on the acquired experience in the small strains realm, it should not be surprising that all these pairs of axial and circumferential, material-dependent, deformations patterns are compatible with the "experimental", highly nonlinear, stresses of Figure 10.*a*. To the best of the authors' knowledge, the present model is the first one that accomplishes such a challenging task.

5. Conclusions

In this paper we analyse the importance of considering transverse strains in orthotropic, incompressible hyperelastic materials undergoing large deformations. We show that neglecting some relevant invariants and, hence, employing an insufficient set of experimental data curves to characterize the material behavior in preferred material axes may result in unrealistic transverse strains. Furthermore, the different material parameters obtained in the parameter-fitting exercise may result in completely different transverse strain evolutions, which may even change sign during deformation. Recent experimental measurements proves the inconsistency of these models with the arterial wall mechanics [37].

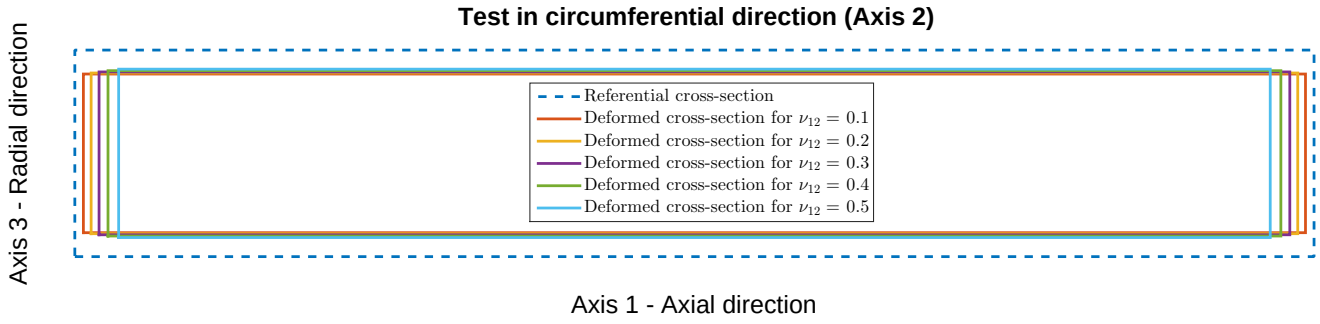

Figure 15: Undeformed and deformed ($\lambda_1 = 1.228$) cross-sectional areas of the stretched circumferential specimen using the model of Section 4 and different prescriptions for ν_{12}.

In contrast, for the WYPIWYG models that we recently presented transverse strains may be prescribed so the model exactly replicates that data along with the remaining stress-strain data. This is possible because the equilibrium and compatibility nonlinear equations of the experiments are exactly solved without imposing the shape of the stored energy terms being proposed, which represent an extension to the nonlinear finite strain case employing logarithmic strains. As a consequence, the physical intuition of the linear theory is preserved within the finite strain regime and the infinitesimal model is recovered in the limit by construction. Then, the transverse strains given by the model in other situations may be predicted beforehand. We remark and have proven that all stress-strain curves, including transverse and shear ones are important in reproducing the actual behavior of a general orthotropic material, regardless of being the response linear or nonlinear and of how exactly they are captured. Thanks to the insight from the linear theory, we have also been able to give herein an improved algorithm for the spline-based model which exactly captures the prescribed finite strain behavior employing neither an optimization procedure nor a user-prescribed parameter guess set.

In 1967, Fung's vision on soft tissue mechanics was that "the main difficulty [in the modelling of soft biological tissues] lies in the customary use of infinitesimal theory of elasticity to the media which normally exhibit finite deformations" [61], see also the excellent review by Humphrey [62]. Today, in our opinion, the main difficulty in modelling soft biological tissues lies in the frequent overlook of infinitesimal theory of elasticity to the media which normally exhibit finite deformations, but which may

equally exhibit infinitesimal deformations as a particular, fundamental case and also in the incremental, general one.

Acknowledgements

Partial financial support for this work has been given by grants DPI2011-26635 and DPI2015-69801-R from the Dirección General de Proyectos de Investigación of the Ministerio de Economía y Competitividad of Spain. F.J. Montáns also acknowledges the support of the Department of Mechanical and Aerospace Engineering of University of Florida during the sabbatical period in which part of this work was performed and Ministerio de Educación, Cultura y Deporte of Spain for the financial suport for that stay under grant PRX15/00065.

References

[1] RM Jones (1975). Mechanics of Composite Materials. McGraw-Hill, New York.

[2] YC Fung (1993). A First Course in Continuum Mechanics. Prentice-Hall.

[3] JD Humphrey (2013). Cardiovascular Solid Mechanics: Cells, Tissues, and Organs. Springer.

[4] RW Ogden (1997) Nonlinear Elastic Deformations. Dover, New York.

[5] M Mooney. A theory of large elastic deformation. Journal of Aplied Physics, 11:582–592. 1940.

[6] RS Rivlin. Large elastic deformations of isotropic materials IV: Further developments of the general theory. Philosophical Transactions of the Royal Society of London A 241(835):379–397. 1948.

[7] PJ Blatz, WL Ko. Application of finite elasticity theory to the deformation of rubbery materials. Transactions of the Society of Rheology 6:223–251. 1962.

[8] OH Yeoh. Characterization of elastic properties of carbon-black-filled rubber vulcanizates. Rubber Chemistry and Technology 63:792–805. 1990.

[9] EM Arruda, MC Boyce. A three-dimensional constitutive model for the large stretch behavior of rubber elastic materials. Journal of the Mechanics and Physics of Solids 41:389–412. 1993.

[10] RW Ogden. Large deformation isotropic elasticity-on the correlation of theory and experiment for incompressible rubberlike solids. In Proceedings of the Royal Society of London A: Mathematical, Physical and Engineering Sciences 326(1567):565–584, 1972

[11] YC Fung, K Fronek, P Patitucci. Pseudoelasticity of arteries and the choice of its mathematical expression. Americal Journal of Physiology 327(5):H620-631, 1979.

[12] CJ Chuong, YC Fung. Three-dimensional stress distribution in arteries. Journal of Biomechanical Engineering 105:268–274, 1983.

[13] JD Humphrey. Mechanics of arterial wall: Review and directions. Critical Reviews in Biomedical Engineering 23, 1–162, 1995.

[14] Y Lanir. Constitutive equations for fibrous connective tissues. Journal of Biomechanics, 16(1), 1-12. 1983

[15] JD Humphrey, FCP Yin. A new constitutive formulation for characterizing the mechanical behavior of soft tissues. Biophysics Journal 52:563–570, 1987.

[16] JD Humphrey, RK Strumpf, FC Yin. Determination of a Constitutive Relation for Passive Myocardium: I. A New Functional Form. Journal of Biomechanical Engineering, 112(3):333–339, 1990.

[17] JD Humphrey, RK Strumpf, FC Yin. Determination of a Constitutive Relation for Passive Myocardium: II.—Parameter Estimation. Journal of Biomechanical Engineering, 112(3):340–346., 1990.

[18] JA Weiss, BN Maker, S Govindjee. Finite element implementation of incompressible, transversely isotropic hyperelasticity. Computer Methods in Applied Mechanics and Engineering, 135(1), 107-128. 1996.

[19] GA Holzapfel, T Gasser, RW Ogden. A new constitutive framework for arterial wall mechanics and a comparative study of material models. Journal of Elasticity, 61:1–18, 2000.

[20] JE Bischoff, EA Arruda, K Grosh. A microstructurally based orthotropic hyperelastic constitutive law. Journal of Applied Mechanics, 69(5), 570-579. 2002.

[21] MS Sacks. Incorporation of experimentally-derived fiber orientation into a structural constitutive model for planar collagenous tissues. Journal of Biomechanical Engineering, 125(2), 280-287. 2003

[22] NJ Driessen, CV Bouten, FP Baaijens. A structural constitutive model for collagenous cardiovascular tissues incorporating the angular fiber distribution. Journal of Biomechanical Engineering, 127(3), 494-503. 2005.

[23] T Gasser, R Ogden, G Holzapfel. Hyperelastic modelling of arterial layers with distributed collagen fibre orientations. Journal of the Royal Society Interface, 3:13–35, 2006.

[24] GA Ateshian, V Rajan, NO Chahine, CE Canal, CT Hung. Modeling the matrix of articular cartilage using a continuous fiber angular distribution predicts many observed phenomena. Journal of Biomechanical Engineering, 131(6), 061003. 2009.

[25] C Flynn, MB Rubin, P Nielsen. A model for the anisotropic response of fibrous soft tissues using six discrete fibre bundles. International Journal for Numerical Methods in Biomedical Engineering, 27(11), 1793-1811. 2011.

[26] G Limbert. A mesostructurally-based anisotropic continuum model for biological soft tissues. Decoupled invariant formulation. Journal of the Mechanical Behavior of Biomedical Materials, 4(8), 1637-1657. 2011.

[27] C Flynn, MB Rubin. An anisotropic discrete fibre model based on a generalised strain invariant with application to soft biological tissues. International Journal of Engineering Science, 60, 66-76. 2012.

[28] GA Holzapfel, JA Niestrawska, RW Ogden, AJ Reinisch, AJ Schriefl. Modelling non-symmetric collagen fibre dispersion in arterial walls. Journal of the Royal Society Interface, 12: 20150188, 2015.

[29] D Li, AM Robertson. A structural multi-mechanism constitutive equation for cerebral arterial tissue. International Journal of Solids and Structures, 46, 2920–2928, 2009.

[30] AJM Spencer (1984). Constitutive theory for strongly anisotropic solids. In Continuum Theory of the Mechanics of Fibre-Reinforced Composites (pp. 1-32). Springer Vienna.

[31] GA Holzapfel (2000). Nonlinear Solid Mechanics. Wiley, Chichester.

[32] GA Holzapfel, RW Ogden. On planar biaxial tests for anisotropic nonlinearly elastic solids. A continuum mechanical framework. Mathematics and Mechanics of Solids, 14: 474–489, 2009.

[33] RW Ogden, G Saccomandi, I Sgura. Fitting hyperelastic models to experimental data. Computational Mechanics, 34(6), 484–502, 2004.

[34] M Latorre, FJ Montáns. Material-symmetries congruency in transversely isotropic and orthotropic hyperelastic materials. European Journal of Mechanics - A/Solids, 53:99–106, 2015.

[35] JG Murphy. Evolution of anisotropy in soft tissue. Procedings of the Royal Society A, 470: 20130548, 2014.

[36] P Sáez, A García, E Peña, TC Gasser, MA Martínez. Microstructural quantification of collagen fiber orientations and its integration in constitutive modeling of the porcine carotid artery. Acta Biomaterialia, in press, Doi: http://dx.doi.org/10.1016/j.actbio.2016.01.030, 2016

[37] P Skacel, J Bursa. Poisson's ratio of arterial wall. Inconsistency of constitutive models with experimental data. Journal of the Mechanical Behavior of Biomedical Materials, 54, 316–327, 2016.

[38] M Latorre, FJ Montáns. On the tension-compression switch of the Gasser–Ogden–Holzapfel model: Analysis and a new pre-integrated proposal. Journal of the Mechanical Behavior of Biomedical Materials, 57, 175–189, 2016.

[39] M Latorre, FJ Montáns. Anisotropic finite strain viscoelasticity based on the Sidoroff multiplicative decomposition and logarithmic strains. Computational Mechanics, 56:503—531, 2015.

[40] M Latorre, FJ Montáns. Fully anisotropic finite strain viscoelasticity based on a reverse multiplicative decomposition and logarithmic strains. Computers & Structures, 163, 56-70, 2016.

[41] M Miñano, FJ Montáns. A new approach to modeling isotropic damage for Mullins effect in hyperelastic materials. International Journal of Solids and Structures, 67-68:272–282, 2015.

[42] M Latorre, FJ Montáns. Extension of the Sussman–Bathe spline-based hyperelastic model to incompressible transversely isotropic materials. Computers & Structures, 122:13–26, 2013.

[43] X Romero, M Latorre, FJ Montáns. Determination of the WYPIWYG strain energy density of skin through finite element analysis of the experiments on circular specimens. Under review.

[44] M Latorre, FJ Montáns. What-You-Prescribe-Is-What-You-Get orthotropic hyperelasticity. Computational Mechanics, 53(6): 1279–1298, 2014.

[45] T Sussman, KJ Bathe. A model of incompressible isotropic hyperelastic material behavior using spline interpolations of tension-compression test data. Communications in Numerical Methods in Engineering, 25(1):53–63, 2009.

[46] ADINA Theory and Modelling Guide. ARD 12-8. ADINA R&D, Watertown, 2012.

[47] M Latorre, FJ Montáns. On the interpretation of the logarithmic strain tensor in an arbitrary system of representation. International Journal of Solids and Structures, 51(7):1507–1515, 2014.

[48] Z Fiala. Discussion of "On the interpretation of the logarithmic strain tensor in an arbitrary system of representation" by M. Latorre and F.J. Montáns. 56–57: 290–291, 2015.

[49] M Latorre, FJ Montáns. Response to Fiala's comments on "On the interpretation of the logarithmic strain tensor in an arbitrary system of representation". International Journal of Solids and Structures 56–57:292, 2015.

[50] P Neff, B Eidel, RJ Martin. Geometry of logarithmic strain measures in solid mechanics. ArXiv:1505.02203 [MathDG]

[51] H Xiao, IO Bruhns, IA Meyers. Logarithmic strain, logarithmic spin and logarithmic rate. Acta Mechanica, 124(1-4): 89-105, 1997.

[52] M Latorre, E DeRosa, FJ Montáns. Understanding the need of the compression branch to characterize hyperelastic materials. Under review.

[53] T Shearer. A new strain energy function for the hyperelastic modelling of ligaments and tendons based on fascicle microstructure. Journal of Biomechanics, 48(2), 290–297, 2015.

[54] A Pandolfi, M Vasta. Fiber distributed hyperelastic modeling of biological tissues. Mechanics of Materials, 44:151–162, 2012.

[55] DH Cortes, DM Elliott. Accurate prediction of stress in fibers with distributed orientations using generalized high-order structure tensors. Mechanics of Materials, 75:73–83, 2014.

[56] A Goriely, M Tabor. Rotation, inversion and perversion in anisotropic elastic cylindrical tubes and membranes. Procedings of the Royal Society A, 469: 20130011, 2013.

[57] AV Melnik, HB Da Rocha, A Goriely. On the modeling of fiber dispersion in fiber-reinforced elastic materials. International Journal of Non-Linear Mechanics, 75:92–106, 2015.

[58] GA Holzapfel, RW Ogden. On the tension-compression switch in soft fibrous solids. European Journal of Mechanics A/Solids, 49:561–569, 2015.

[59] EA Kearsley, LJ Zapas. Some Methods of Measurement of an Elastic Strain-Energy Function of the Valanis-Landel Type. Journal of Rheology, 24(4):483–500, 1980.

[60] YC Fung (1993). Biomechanics: Mechanical Properties of Living Tissue. Springer-Verlag, New York, 2nd edn.

[61] YCB Fung. Elasticity of soft tissues in simple elongation. American Journal of Physiology, 213(6):1532–1544, 1967.

[62] JD Humphrey. Review Paper: Continuum biomechanics of soft biological tissues. Proceedings of the Royal Society of London A, 459:3–46, 2003.